



## In Situ Crystallographic Probing on Ameliorating Effect of Sulfide Additives and Carbon Grafting in Iron Electrodes

M. K. Ravikumar,<sup>a,\*</sup> A. Sundar Rajan,<sup>a</sup> S. Sampath,<sup>b</sup> K. R. Priolkar,<sup>c</sup> and A. K. Shukla<sup>a,\*\*\*z</sup>

<sup>a</sup>Solid State and Structural Chemistry Unit, Indian Institute of Science, Bangalore 560012, India

<sup>b</sup>Department of Inorganic and Physical Chemistry, Indian Institute of Science, Bangalore 560 012, India

<sup>c</sup>Department of Physics, Goa University, Taleigao Plateau, Goa 403 206, India

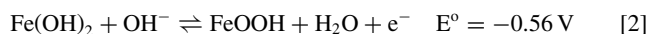
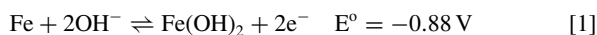
Beneficial effects of carbon grafting into the iron active material for rechargeable alkaline-iron-electrodes with and without Bi<sub>2</sub>S<sub>3</sub> additive is probed by in situ X-ray diffraction in conjunction with Extended X-ray Absorption Fine Structure (EXAFS) and electrochemistry. EXAFS data unravel that the composition of pristine active material (PAM) for iron electrodes comprises 87% of magnetite and 13% of  $\alpha$ -iron while carbon-grafted active material comprises 60% of magnetite and 40% of  $\alpha$ -iron. In situ XRD patterns are recorded using a specially designed electrochemical cell. XRD data reflect that magnetite present in PAM iron electrode, without bismuth sulfide additive, is not reduced during charging while PAM iron electrode with bismuth sulfide additive is partially reduced to  $\alpha$ -Fe/Fe(OH)<sub>2</sub>. Interestingly, carbon-grafted-iron electrodes with bismuth sulfide exhibit complete conversion of active material to  $\alpha$ -Fe/Fe(OH)<sub>2</sub>. The ameliorating effect of carbon grafting is substantiated by kinetic parameters obtained from steady-state potentiostatic polarization and Tafel plots. The mechanism for iron-electrode charge – discharge reactions are discussed in the light of the potential – pH diagrams for Fe – H<sub>2</sub>O, S – H<sub>2</sub>O and FeS<sub>ads</sub> – H<sub>2</sub>O systems and it is surmised that carbon grafting into iron active material promotes its electrochemical utilization.

© The Author(s) 2015. Published by ECS. This is an open access article distributed under the terms of the Creative Commons Attribution 4.0 License (CC BY, <http://creativecommons.org/licenses/by/4.0/>), which permits unrestricted reuse of the work in any medium, provided the original work is properly cited. [DOI: 10.1149/2.0721512jes] All rights reserved.

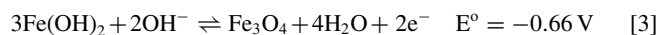
Manuscript submitted June 24, 2015; revised manuscript received August 14, 2015. Published September 17, 2015. This was Paper 20 presented at the Chicago, Illinois, Meeting of the Society, May 24–28, 2015.

Commercialization of a battery technology depends largely on the availability of its constituent materials in conjunction with their environmental compatibility, safety and cost. Iron is non-toxic, low-cost and environmentally safe material; it also has theoretical specific capacity of 0.96 Ah/g. Iron electrode was first developed independently by Jünger in Europe and Edison in US for realizing alkaline Ni-Fe batteries. Iron electrodes developed by Edison were robust to overcharge and discharge, temperature abuse, and mechanically rugged with shelf-life in excess of 10 years.<sup>1,2</sup> Although the use of iron as negative electrode for alkaline Ni-Fe batteries is known for more than a century, the problems associated with iron electrodes have prevented the practical exploitation of iron-based accumulators. The major problems limiting the capacity and cycle-life of rechargeable-alkaline-iron electrodes are passivation due to corrosion and the associated hydrogen-evolution reaction.

Alkaline iron-electrodes undergo discharge in two steps. The first step of discharge reaction involves oxidation of metallic iron to ferrous hydroxide with a theoretical specific capacity of 0.96 Ah/g. The second step of discharge reaction results in further oxidation of ferrous hydroxide to iron oxy-hydroxide with a theoretical capacity of 0.298 Ah/g. These reactions with their standard electrode potentials are represented as:



Magnetite is also a favorable product in concentrated alkali during the second step of discharge according to Eq. 3.<sup>1</sup>

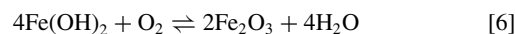


The open-circuit potential for a charged alkaline-iron-electrode is always negative to hydrogen-evolution reaction in the same solution. Consequently, iron is thermodynamically unstable and suffers corrosion with concomitant hydrogen-evolution reaction. Hydrogen evolution also occurs while charging the alkaline iron-electrode manifesting as a decrease in its charge acceptance. In addition, the reduction of aerial oxygen dissolved in the electrolyte is also a conjugate reaction

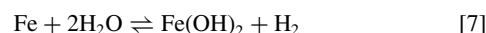
as shown below.



Accordingly, iron could undergo corrosion due to the dissolved oxygen and form passive corrosion products, namely ferrous hydroxide, magnetite, ferric oxide.



Ferrous hydroxide can also be produced due to hydrogen evolution reaction as shown below and nature of corrosion products depends on the operating environment of iron electrode.



As a consequence of hydrogen evolution and corrosion reactions, alkaline iron-electrodes exhibit low charge-acceptance, poor charge-retention, and low specific-capacity with reduced cycle-life. The performance of alkaline iron-electrode can be improved by modifying its structure and composition using porous electrodes and additives that could reduce rate of parasitic reactions. In the literature, it is reported that a mixture of  $\alpha$ -iron and magnetite is used as active material for iron electrodes.<sup>3</sup> Among the various additives, Li<sup>+</sup> and S<sup>2-</sup> ions are known to have beneficial effects on the performance of iron electrodes.<sup>4-8</sup> In the literature, sulfide additives that have been used to increase hydrogen overpotential are iron (II) sulfide, lead (II) sulfide and bismuth sulfide.<sup>9-11</sup>

We have reported earlier that thermal decomposition of ferrous oxalate dihydrate results in a mixture of  $\alpha$ -Fe and magnetite.<sup>9</sup> It is used as active material and labeled as pristine active material (PAM) for iron electrodes. These iron electrodes with bismuth sulfide additive delivered a specific capacity between 250 and 300 mAh/g at C/3 to C/5 rate. Recently, we have reported an in situ carbon-grafted, alkaline iron electrode for iron-based accumulators with specific capacity values in excess of 400 mAh/g and faradaic efficiency of about 80% at C/10, C/5, C/2 rate; even at C and 2C rates, respective specific discharge capacity values of 376 mAh/g and 322 mAh/g are obtained with respective faradaic efficiency values of 75% and 64%.<sup>12</sup>

In this communication, we report the ameliorating effect of sulfide additives and carbon grafting into the iron active material on its kinetics and mechanism. We have conducted these studies by in situ X-ray diffraction in conjunction with EXAFS, and potentiostatic

\*Electrochemical Society Active Member.

\*\*Electrochemical Society Fellow.

<sup>z</sup>E-mail: akshukla2006@gmail.com

and galvanostatic polarization techniques for PAM iron electrodes with and without bismuth sulfide additives, and carbon grafted active material (CGAM) iron electrodes with bismuth sulfide additive. A detailed systematic study is carried out on the crystalline structure of iron electrodes at varying state-of-charge values to understand the role of carbon grafting and sulfide additives in porous alkaline-iron-electrodes. In situ XRD patterns for all the iron electrodes in as prepared state reflect that electrodes initially contain a mixture of  $\alpha$ -iron and magnetite. PAM iron electrodes without bismuth sulfide additive at state-of-charge (SoC)  $\sim$  100% show the presence of only  $\alpha$ -iron and magnetite. In situ XRD data for discharge products in PAM iron electrode without bismuth sulfide recorded at varying SoCs suggest that iron is directly oxidized to magnetite subsequent to the formation cycles. In PAM electrode with bismuth sulfide additive at SoC  $\sim$  100% and after its constant current discharge to  $-0.8$  V vs. MMO, XRD data exhibit the presence of  $\alpha$ -iron, ferrous hydroxide and magnetite. Interestingly, in carbon grafted active material (CGAM) iron electrode with bismuth sulfide additive at a similar SoC, XRD data depicts the presence of only iron and ferrous hydroxide.

The role of sulfide additives has been studied earlier but these studies are not fully conclusive. Recently, Narayanan et al. have reported that conductive phase of sparingly soluble iron (II) sulfide prevents rapid passivation of iron electrode during discharge and sulfide ions reduce overpotential for the conversion of magnetite to metallic iron.<sup>13</sup> The present study also reflects that sulfide ions from bismuth sulfide have bi-functional role both in charging and discharging reactions of iron electrodes. Beneficial effects of bismuth sulfide additives are that (a) it promotes the reduction of magnetite to iron and hence capacity of iron electrode is increased, (b) it stabilizes and facilitates precipitation of crystalline ferrous hydroxide, (c) it prevents the formation of magnetite during the first step of discharge reaction, and (d) it enhances the cycle life of iron electrodes. CGAM iron electrode with bismuth sulfide additive shows complete reduction of magnetite at the end of formation cycles indicating that carbon grafted into the iron active material promotes utilization of the active material. A mechanism has been proposed to explain these beneficial effects of sulfide ions.

## Experimental

**Preparation of active materials and iron electrodes.**— The preparation procedure used is akin to that reported earlier.<sup>12</sup> In brief, pristine active material (PAM) was prepared by decomposing  $\alpha$ -ferrous oxalate dihydrate at  $600^\circ\text{C}$  under dynamic vacuum. CGAM was prepared by decomposing a mixture of  $\alpha$ -ferrous oxalates dihydrate with 10 wt% polyvinyl alcohol (PVA) at  $600^\circ\text{C}$  under dynamic vacuum. Electrodes of required size for in situ electrochemical cell were prepared as follows. PAM iron electrode without any additive was prepared by mixing 83.5 wt% of PAM, 10 wt% of graphite powder, 0.5 wt%  $\text{NiSO}_4 \cdot 7\text{H}_2\text{O}$  in aqueous potassium hydroxide to form a homogeneous slurry to which 6 wt% of 60 wt% polytetrafluoroethylene (PTFE) dispersion in water was added. The resulting paste like mass was spread onto a degreased nickel mesh and compacted at a pressure of  $675 \text{ kg/cm}^2$  for 5 min. Typical size of an electrode was  $2.8 \text{ cm} \times 3 \text{ cm}$  with thickness of about 1 mm. In case of PAM iron and CGAM iron electrodes with bismuth sulfide additive, 82.5 wt% of active material, 10 wt% of graphite powder, 1 wt% of bismuth sulfide, 0.5 wt% of  $\text{NiSO}_4 \cdot 7\text{H}_2\text{O}$  was dispersed in aqueous potassium hydroxide to which 6 wt% of 60 wt% PTFE dispersion in water was added. All the electrodes were sintered at  $350^\circ\text{C}$  for 30 min under nitrogen stream. Subsequently, electrodes were cooled and assembled into formation cells. Formation cycling was conducted in a 3-electrode electrochemical cell with sintered-type commercial nickel oxy-hydroxide as counter electrodes on either side of the working iron electrode and a mercury-mercuric oxide (MMO) reference electrode.

**Electrochemical formation and characterization of Fe electrodes.**— Formation cells connected to an eight channel potentiostat/galvanostat model 1470E from Solartron Analytical (UK). PAM iron electrode without bismuth sulfide were charged

at  $100 \text{ mA/g}$  for 5 h and discharged at the same current density to a cutoff potential of  $-0.8$  V vs. MMO. The same electrode was again charged and assembled into a 3-electrode specially designed electrochemical cell for in situ XRD investigations. In case of PAM and CGAM iron electrodes with bismuth sulfide additive, electrodes were subjected to formation cycles by charging at  $100 \text{ mA/g}$  and discharging them at the same current density to a cutoff potential of  $-0.8$  V vs. MMO until a stable capacity was obtained. Steady-state potentiostatic and galvanostatic polarization measurements were carried out in the formation cells on fully-formed electrodes at SoC 100%. Steady-state potentiostatic polarization measurements were carried out with iron electrodes first in the anodic direction by applying potential steps of 25 mV for 5 min duration at each potential in the potential range between  $-1.2$  V and  $-0.2$  V vs. MMO. Subsequently, the electrodes were polarized in the cathodic direction following the same sequence. Galvanostatic current – potential curve were obtained by applying anodic current in the range from  $10 \mu\text{A}$  to  $1 \text{ A}$  range for duration of 5 min for each selected load current. The uncompensated ohmic resistance was determined by current-interrupter method and the data was mass-transfer corrected following the standard methods.<sup>14</sup> Potentiostatic and galvanostatic studies were carried out in the formation cells.

**EXAFS characterization of PAM and CGAM.**— EXAFS spectra for PAM, CGAM and iron metal powders were recorded using scanning EXAFS beam line (BL 9) at INDUS-II Synchrotron source (India) in transmission mode using absorbers made from finely ground powder uniformly distributed on a scotch tape. Such sample coated strips were adjusted in number such that the absorption edge jump gave  $\Delta\mu \leq 1$ , where  $\Delta\mu$  is the change in absorption coefficient at the absorption edge and  $t$  is the thickness of the absorber. Incident and transmitted photon energies were simultaneously recorded using gas-ionization chambers as detectors. Measurements were carried out from 200 eV below the edge energy to 800 eV above it. Data analysis was carried out using Demeter analysis program.<sup>15</sup> Theoretical fitting standards were computed with FEFF6.<sup>16</sup> Data in the  $k$ -range of  $3\text{--}12 \text{ \AA}^{-1}$  and  $R$ -range of  $1\text{--}3 \text{ \AA}$  were used for analysis.

**In situ X-ray diffraction characterization.**— An in-house built 3-electrode electrochemical cell was used for recording in situ X-ray diffraction patterns for the iron electrodes is shown in Fig. 1.<sup>17</sup> The cell was assembled with sintered type commercial nickel oxy-hydroxide counter electrodes and MMO as reference electrode. Working electrode was mounted horizontally on the working electrode support as shown in Fig. 2. Electrolyte level in the cell was adjusted so as to have a thin layer of electrolyte on the electrode surface. The cell was designed in such way as to place the luggin tip of the reference electrode at an appropriate distance from the working electrode. The top of the cell was covered with Kapton film avoiding its contact with aqueous potassium hydroxide electrolyte. Brüker D8 Discover model X-ray diffractometer fitted with UMC 1516 sample stage and Co radiation source was used to record all powder and in situ XRD patterns. In situ XRD cell mounted on UMC 1516 sample stage of X-ray diffractometer is shown in Fig. 2. Height of sample stage was then adjusted to align working electrode, X-ray source and detector using software while in situ XRD cell was placed on the sample stage. This alignment procedure was carried out independently for each electrode. In situ electrochemical cell was connected externally to an Autolab PGSTAT 302N to perform charge and discharge reactions of the iron electrode.

In situ XRD patterns were recorded at specific state-of-charge values in the following sequence, namely as prepared electrodes before subjecting them to formation cycles, subsequent to their formation at open-circuit potential in fully-charged state (SoC  $\sim$  100%), at the end of 1<sup>st</sup> step of discharge with a cutoff potential of  $-0.8$  V vs. MMO by keeping the cell undisturbed and at the end of 2<sup>nd</sup> step of discharge with a cutoff potential of  $-0.1$  V vs. MMO keeping the cell undisturbed. Powder XRD patterns for PAM, CGAM and graphite powder were also recorded. In order to understand charge and

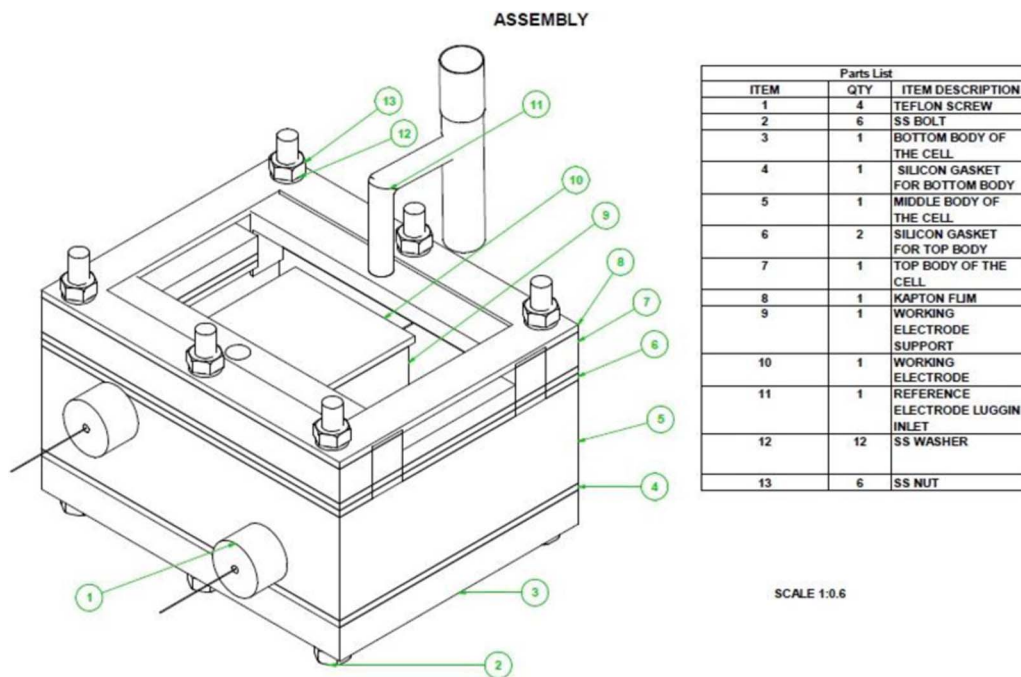


**Figure 1.** Schematic representation of in situ electrochemical cell.

discharge mechanisms of the iron-electrode additives, additional XRD patterns were also recorded after potentiostatic polarization measurements wherever desired. All powder and in situ XRD patterns for the iron electrodes were recorded for Bragg angle ( $\theta$ ) range between  $5^\circ$  and  $60^\circ$  at about  $1^\circ/\text{min}$  scan rate. All the collected data were corrected for  $\text{CoK}\alpha_2$  lines with noise and background subtracted for further phase analyses. Phase analyses were carried out by profile matching mode. A representative matching XRD-pattern is shown in Fig. 1 under Supplementary Information.

### Results and Discussion

**Powder XRD characterization of active materials.**— Powder XRD patterns for PAM, CGAM and graphite powder used for electrode preparation are shown in Figs. 3a–3c. Fig. 3a shows carbon in hexagonal crystal system suggesting it to be crystalline graphitic-carbon. Phase analysis of powder XRD pattern for PAM and CGAM shown in Figs. 3b and 3c is the best fit for the combination of  $\alpha$ -iron in body cen-

tered cubic (bcc) crystal system with space group Im3m and magnetite in face centered cubic (fcc) crystal system with space group Fd-3m. Reflections from various crystal planes are indexed with reference to PDF Nos. 00-026-1080 for Carbon, 00-006-0696 for  $\alpha$ -iron and 00-019-0629 for magnetite. Relative intensities for PAM and CGAM suggest magnetite as the dominant phase in PAM while  $\alpha$ -iron is the dominant phase in CGAM. This is in accordance with our earlier report that the PVA added to the ferrous oxalate thermally decomposes to form carbonaceous products and is utilized for the reduction of magnetite to  $\alpha$ -iron providing higher content of metallic iron in the active material.<sup>12</sup>

**EXAFS characterization of PAM and CGAM.**— Powder XRD patterns show that PAM and CGAM are mixtures of metallic iron and magnetite. Average composition for these is determined from EXAFS of PAM and CGAM. Background-subtracted EXAFS data and their Fourier transform are shown in Figs. 4a–4d. The EXAFS data were fitted by varying the relative composition of magnetite and iron while keeping the coordination number and bond distances constant. The best fitted data suggest that PAM has an average composition of 87% of magnetite and 13% of  $\alpha$ -iron while CGAM has 60% of magnetite and 40% of  $\alpha$ -iron. Averaging is performed using various samples of CGAM prepared from different compositions of PVA and ferrous oxalate.

**Steady-state potentiostatic polarization data for iron electrodes.**— Steady-state potentiostatic polarization data for the electrodes, namely PAM iron electrode without bismuth sulfide, PAM iron, and CGAM iron electrode with bismuth sulfide, are shown in Fig. 5. All the three iron electrodes show two active – passive transitions in the anodic direction of polarization corresponding to two discharge reactions of iron electrodes. In the case of PAM iron electrode without bismuth sulfide, the steady-state potentiostatic polarization is carried out after the first charge of the electrode at 100 mA for 5 h. In case of other two electrodes, potentiostatic polarization is carried out on fully-formed electrode at  $\text{SoC} \sim 100\%$ . The critical current ( $i_{\text{crit}}$ ), passivation potential ( $E_p$ ) and breaking potentials ( $E_b$ ) obtained for first active – passive transition are presented in Table I. The breaking potential listed in the Table I represents the breaking of passive layer formed during the first step of discharge product, namely ferrous hydroxide. It is observed

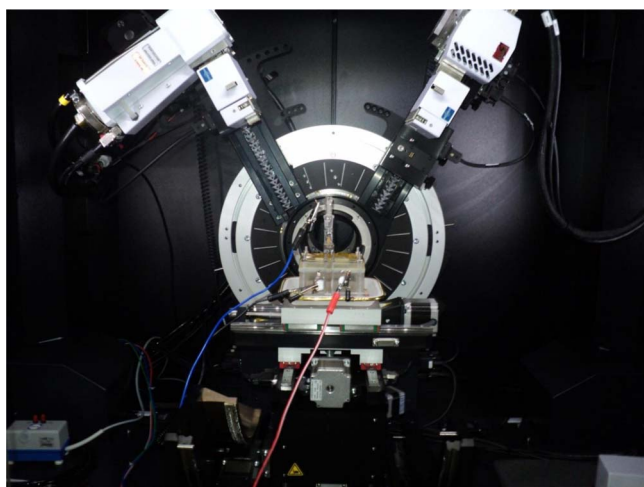


**Figure 2.** In situ electrochemical cell mounted in the XRD.

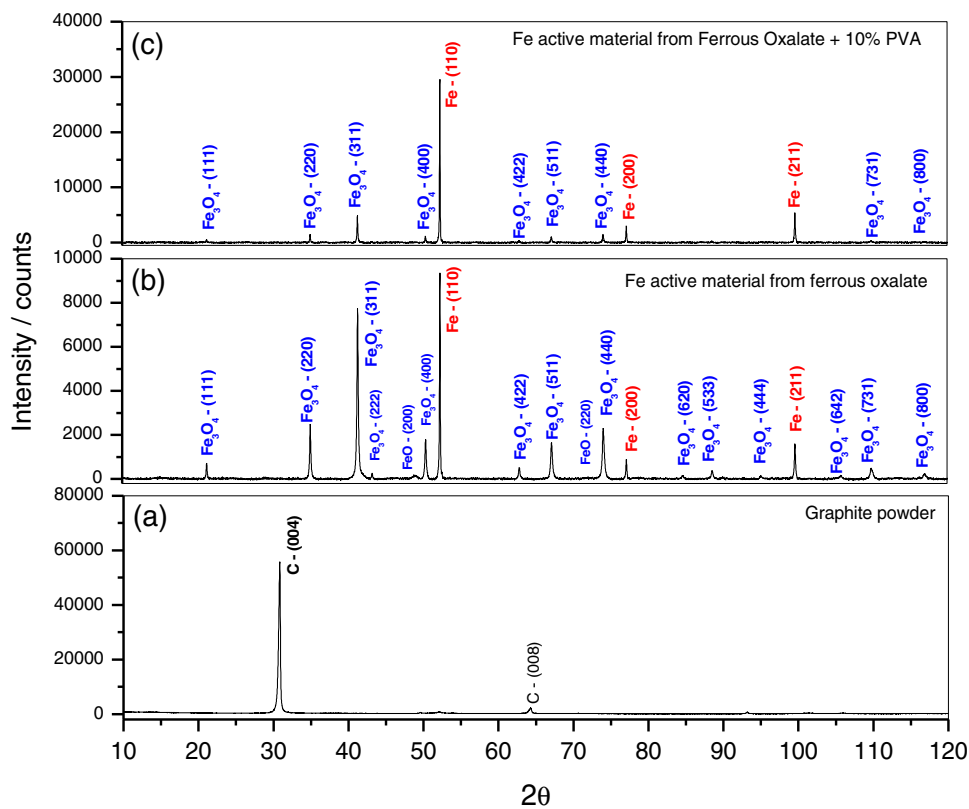


**Figure 3.** Powder XRD patterns for (a) graphite powder, (b) iron active material from ferrous oxalate (PAM) and (c) iron active material from ferrous oxalate and 10 wt% PVA (CGAM).

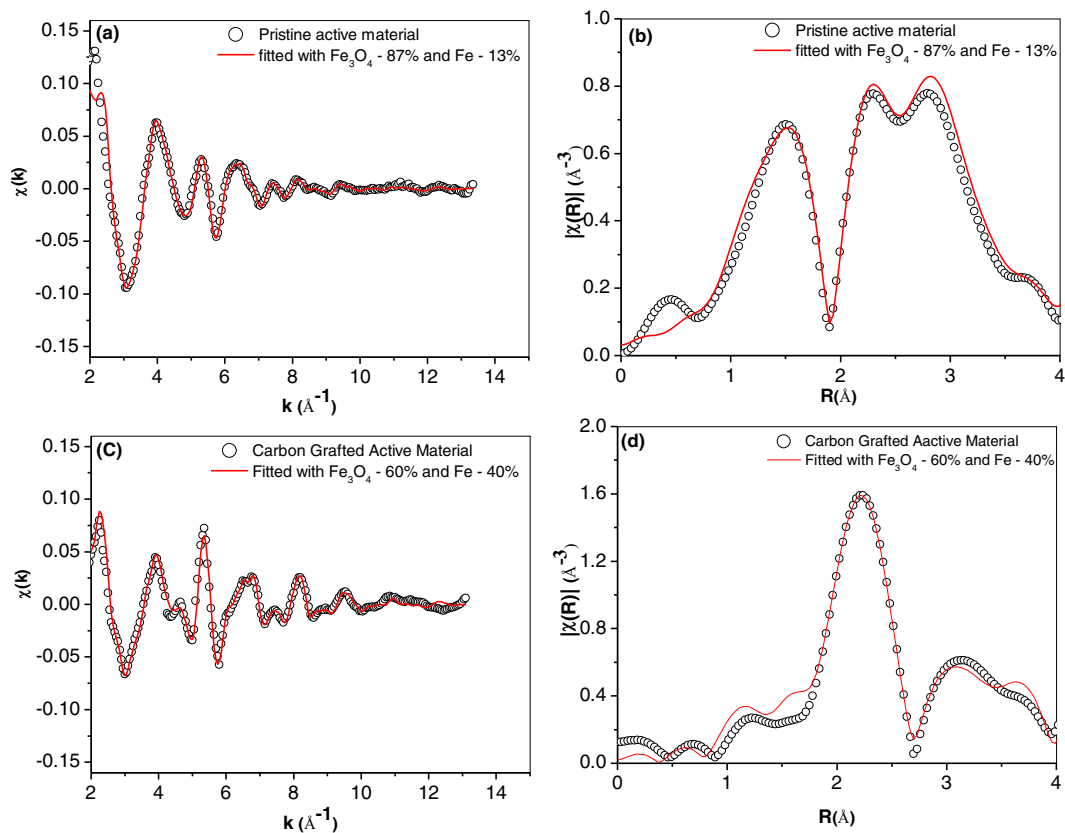


**Figure 4.** EXAFS data for (a) PAM and (b) its FT data, and (c) CGAM and (d) its FT data.

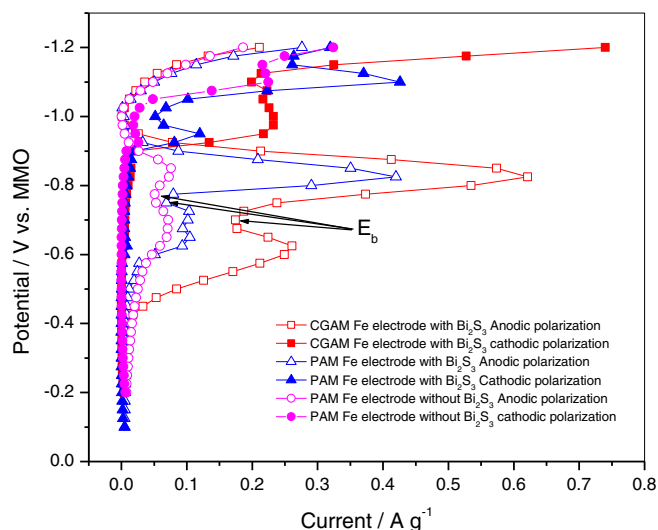


**Figure 5.** Steady-state potentiostatic polarization data for iron electrodes.

that the passivation potential is almost same for all the three electrodes while the passive film breaking potential is shifted to more anodic potentials for bismuth sulfide added electrodes, and is maximum for CGAM iron electrodes. In other words, the sulfide additives stabilize ferrous hydroxide layer and prevent its oxidation to magnetite at the end of first step of discharge. The critical current values are found to be 0.07 A, 0.414 A and 0.618 A, respectively, for the three electrodes with maximum  $I_{crit}$  for CGAM iron electrode. This suggests that both bismuth sulfide and carbon have positive effect on the capacity of the iron electrode in the first discharge step as represented in Eq. 1. Two cathodic peaks are observed during the cathodic polarization of the iron electrodes. These peaks correspond to the reduction of magnetite to ferrous hydroxide and reduction of ferrous hydroxide to metallic iron. These are confirmed by in situ XRD patterns recorded after constant potential polarization on a deeply discharged iron electrodes and explained in a latter section. The onset potential for reduction of passive film is observed at  $-0.9$  V for all the three electrodes but the current is higher for CGAM iron electrode with bismuth sulfide. The  $I_{red}$  for the first cathodic peak is presented in the Table I.  $I_{red}$  for the second cathodic peak is not included as the current is contributed by both the iron reduction and hydrogen evolution reactions;  $I_{red}$  for the first cathodic peak shows the reduction of magnetite to ferrous hydroxide.

*Steady-state galvanostatic polarization of iron electrodes.*— Steady-state galvanostatic polarization data in anodic direction for the three electrodes at SoC  $\sim 100\%$  are presented in Fig. 6. These data are corrected for uncompensated ohmic resistance and mass-transfer effects. Tafel slopes obtained from these plots are presented in Table I. It is observed that the Tafel slopes for PAM iron electrode and CGAM iron electrodes are similar indicating no significant change in iron

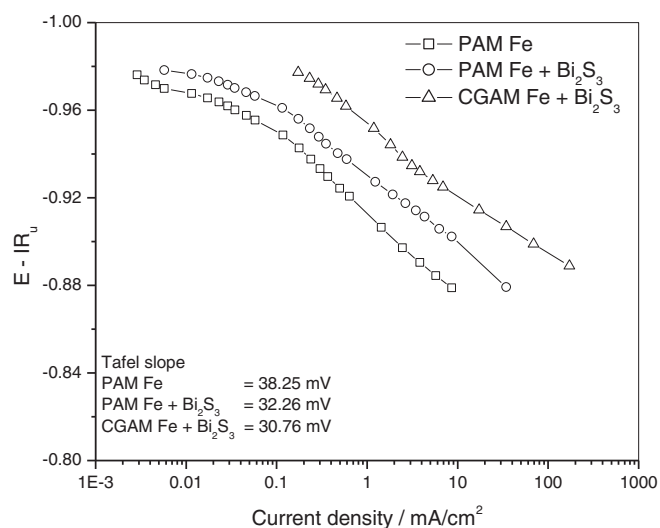


**Figure 6.** Galvanostatic polarization data after correcting for mass transfer effect and uncompensated ohmic resistance. Tafel slopes are estimated from the data between  $0.1 \text{ mA/cm}^2$  and  $10 \text{ mA/cm}^2$ .

electrode reactions due to carbon grafting. However, the electrodes with carbon grafting show high current performance due to the presence of higher amount of metallic iron. As stated earlier, PVA added during the preparation of CGAM undergoes thermal decomposition producing carbonaceous substances that are utilized for reduction of magnetite to  $\alpha$ -iron. In addition, carbon is grafted uniformly over the active material. Hence, CGAM iron electrodes have more metallic iron with uniformly distributed carbon. As a result, these electrodes exhibit high critical current.

*In situ XRD characterization of as prepared electrodes.*— In situ XRD patterns for all the three electrodes assembled in a newly designed in situ electrochemical cell in as prepared state are shown in Figs. 7a–7c. These patterns show the combined XRD for graphite powder with PAM and CGAM. We could not see the presence of bismuth sulfide as it is present in very low amounts in these electrodes. There is no other change in XRD for as prepared electrodes in relation to the powder active material suggesting that the active material is unaffected during electrode preparation.

*In situ electrochemical and XRD characterization of PAM Fe electrode without bismuth sulfide.*— Constant-current-discharge data for the first and second steps for the PAM iron electrode without bismuth sulfide in in situ XRD cell are shown in Figs. 8a and 8b. The (\*) mark in the figure shows the state-of-charge for which XRD patterns are recorded. In Fig. 8a, the first step of discharge curve shows an initial drop in the potential from  $-0.97$  V to about  $-0.84$  V vs. MMO but subsequently there is no significant change in potential during the discharge of iron electrode. The decrease in potential is attributed to

**Table I.** Kinetic parameters for various iron electrodes.

Electrode	Active to passive transition parameters during potentiostatic polarization in the anodic direction			Reduction of passive film during potentiostatic polarization in the cathodic direction		Tafel slope from galvanostatic polarization measurements
	$I_{crit}/\text{A}$	$E_p/\text{V vs. MMO}$	$E_b/\text{V vs. MMO}$	$I_{red}/\text{A}$	$E_R/\text{V}$	mV
PAM Fe	0.07	$-0.834$	$-0.766$	0.02	$-0.933$	38.25
PAM Fe with $\text{Bi}_2\text{S}_3$	0.414	$-0.824$	$-0.749$	0.121	$-0.943$	32.26
CGAM Fe with $\text{Bi}_2\text{S}_3$	0.618	$-0.825$	$-0.690$	0.231	$-0.996$	30.76

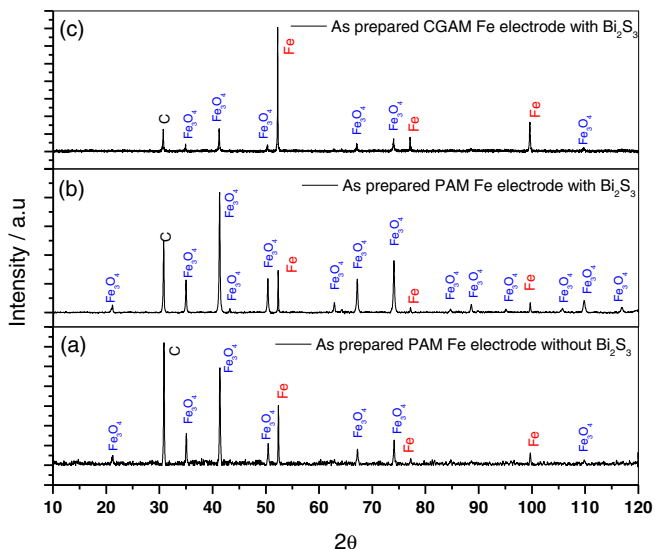


**Figure 7.** In situ XRD for as prepared (a) PAM iron electrode without bismuth sulfide, (b) PAM with bismuth sulfide and (c) CGAM iron electrode with bismuth sulfide.

ohmic resistance of the cell. The discharge profile subsequent to the ohmic drop suggests that the first step of discharge for iron electrode involves dissolution – precipitation mechanism. The electrode delivers a capacity of 55.6 mAh/g at the discharge current of 40 mA. The same electrode after recording the XRD is further discharged for the second step of discharge of iron electrode and the discharge curve is shown in Fig. 8b. Iron electrode potential is found to vary linearly with time during the second step of discharge. This suggests that the second step of discharge for iron electrode involves a homogeneous

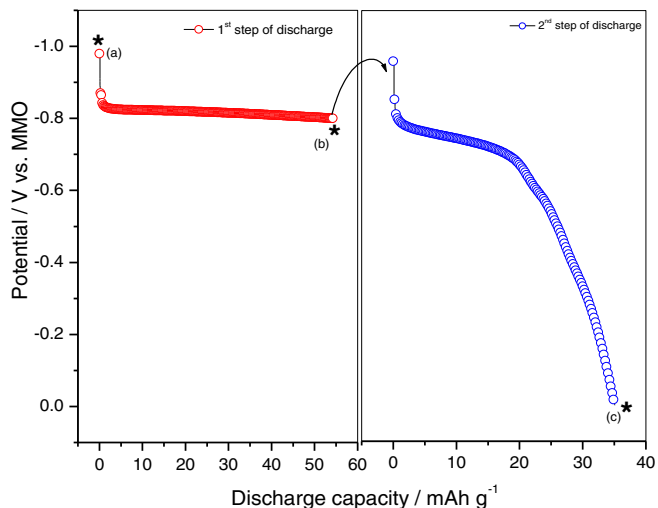


**Figure 8.** Constant-current discharge curves of PAM iron electrodes without bismuth sulfide at 40 mA in the in situ XRD cell.

mechanism. The electrode has delivered a discharge capacity of 35 mAh/g. In situ XRD patterns for a new and fully-charged PAM iron electrode without bismuth sulfide at open-circuit potential of  $-0.97$  V vs. MMO, after constant-current discharge at 40 mA to the end of 1<sup>st</sup> step of discharge reaction with a cutoff potential of  $-0.8$  V vs. MMO and after the end of 2<sup>nd</sup> step of discharge reaction with a cutoff potential of  $-0.0$  V vs. MMO are shown in Figs. 9a–9c. XRD patterns at OCP  $-0.97$  V vs. MMO at SoC  $\sim 100\%$  and after the end of 1<sup>st</sup> step of discharge show the presence of both magnetite and  $\alpha$ -iron phases. However, at the end of 1<sup>st</sup> step of discharge, the intensity of magnetite phase is increased. These XRD patterns also show some additional peaks marked as (\*). There is no significant change in the intensity

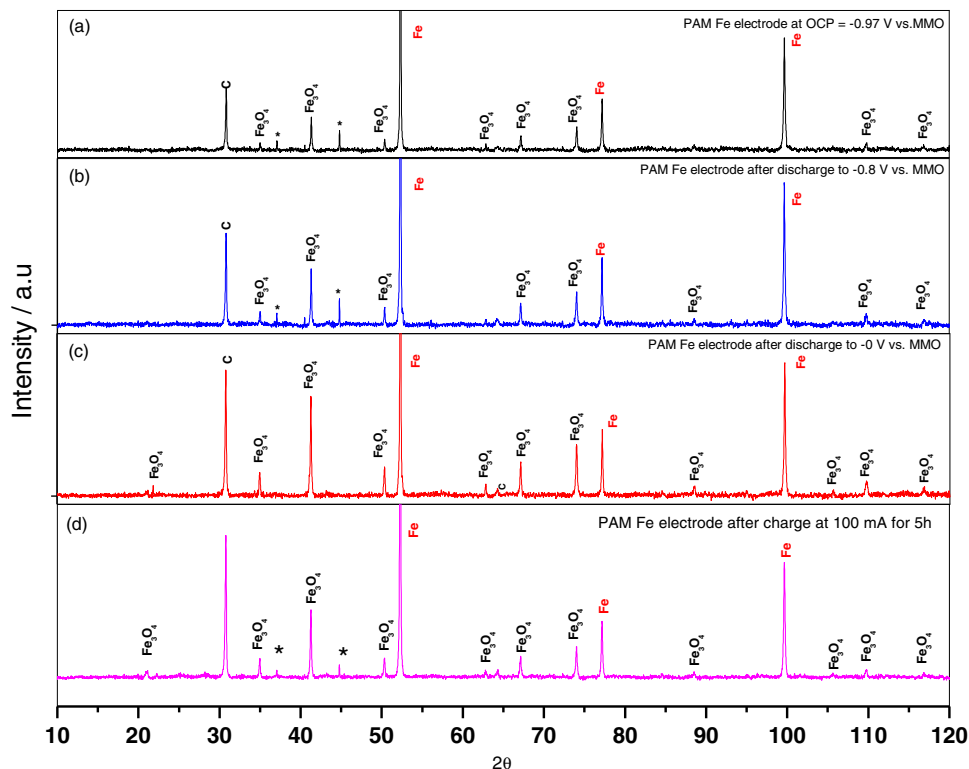


**Figure 9.** In situ XRD for PAM iron electrode without bismuth sulfide during constant current discharge at (a) OCP, (b) after discharge to  $-0.8$  V vs. MMO, (c) after discharge to 0 V vs. MMO and (d) after charging at 100 mA for 5 h.

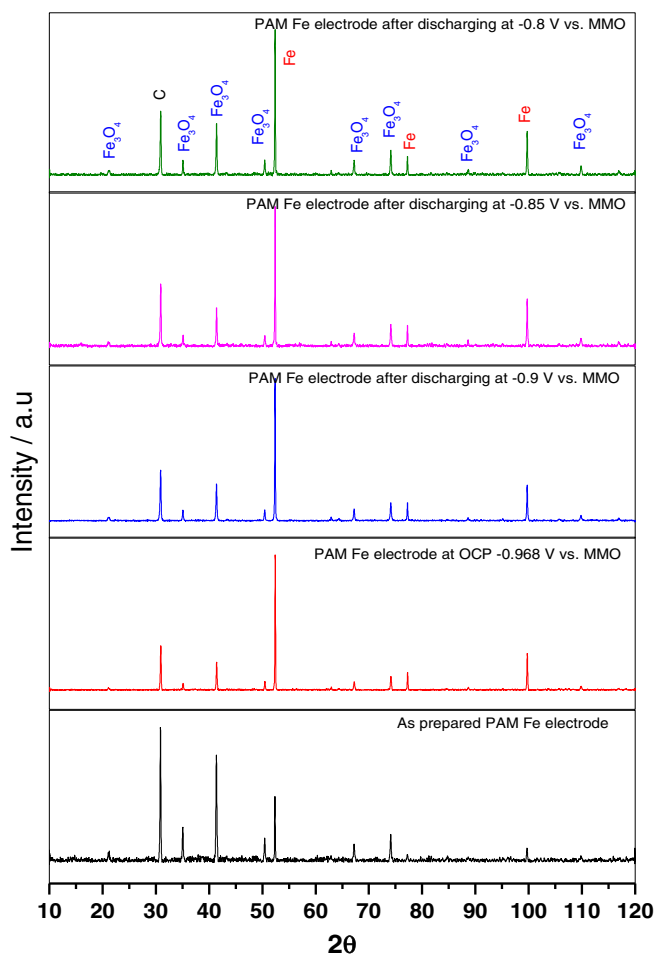


**Figure 10.** In situ XRD for PAM iron electrode without bismuth sulfide during potentiostatic polarization in the anodic direction at various potentials.

of these peaks during the first step of discharge. But the XRD pattern after the end of 2<sup>nd</sup> step of discharge shows further increase in the intensity of magnetite phase and the additional peaks marked as (\*) disappear. This suggests that the additional peaks observed at OCP and at the end of first step of discharge are due to corrosion products of iron. XRD patterns recorded at varying state-of-charge values do not show the presence of ferrous hydroxide according to the first step of discharge reaction of iron electrode shown in Eq. 1. This could be due to charge and discharge cycling in the formation cycles. In literature, it has been reported that repeated charge and discharge cycles results in gradual conversion of crystalline ferrous hydroxide to more stable magnetite.<sup>18</sup>

During constant-current discharge of PAM Fe – electrode, potential dropped below  $-0.84$  V vs. MMO but the steady-state potentiostatic polarization data shown in Fig. 5 for PAM Fe – electrode without bismuth sulfide indicate that the first step of discharge for iron starts from  $-0.9$  V vs. MMO. In order to find the nature of discharge product in this potential regime, a newly prepared PAM iron – electrode without bismuth sulfide is charged at a constant current of 100 mA/g current density for five hours and then discharged at constant potentials of  $-0.9$  V,  $-0.85$  V and  $-0.8$  V vs. MMO. The electrode is discharged for 2 h at each discharge potential steps. In situ XRD recorded after each of the discharge steps and the data are shown in Fig. 10. These XRD patterns also show the presence of only  $\alpha$ -iron and magnetite phases with no indication of crystalline ferrous hydroxide.

In situ XRD pattern for the discharge products during the first step of discharge for the PAM iron electrode without bismuth sulfide additive obtained by both constant-current discharge and constant-

potential discharge indicate no formation of crystalline ferrous oxide but it may be present in amorphous state or in a quantity too low to be detected by XRD. This could as well be due to repeated cycling of the iron electrode as reported in the literature.<sup>18</sup> The increase in intensity of the peaks due to magnetite suggests that ferrous hydroxide could be easily oxidized to magnetite. In other words, PAM Fe electrodes without bismuth sulfide additives are easily passivated.

*In situ electrochemical and XRD characterization of PAM Fe electrode with Bi<sub>2</sub>S<sub>3</sub>.*— Constant-current discharge data during the first and second step for PAM iron electrode with bismuth sulfide are shown in Figs. 11a and 11b. This electrode delivered a capacity of 284 mAh/g and 213 mAh/g during first and second step of discharge, respectively. The (\*) mark in the figures show that state-of-charge values for which in situ XRD patterns are recorded. In situ XRD patterns recorded for fully-formed PAM iron electrode with bismuth sulfide in fully charged condition (SoC  $\sim$  100%) at OCP, end of 1<sup>st</sup> step and at the end of 2<sup>nd</sup> step of discharge are shown in Figs. 12a–12c. PAM Fe electrode with bismuth sulfide shows (a) the presence of  $\alpha$ -iron and magnetite at OCP, (b)  $\alpha$ -iron, ferrous hydroxide and magnetite at the end of 1<sup>st</sup> step and (c)  $\alpha$ -iron and magnetite at the end of 2<sup>nd</sup> step of discharge. Ferrous hydroxide is formed in hexagonal crystal system belonging to the space group P-3m1. The reflections from various crystal planes were indexed with reference to PDF No. 00-013-0089. The intensity of reflections from magnetite phase increases at the end of 2<sup>nd</sup> step of discharge. XRD pattern also shows few additional peaks but their intensities do not change during the discharge of iron electrode. This indicates that these could be due to emergence of passive corrosion products akin to iron oxyhydroxide during formation of the iron electrode. The increased capacity for PAM iron electrode with bismuth sulfide compared to the PAM iron electrode without bismuth sulfide indicate that bismuth sulfide additive catalyses the reduction of magnetite to  $\alpha$  – Fe. The presence of ferrous hydroxide at the end of 1<sup>st</sup> step of discharge indicates that the precipitation of discharge product ferrous hydroxide is facilitated by the presence of bismuth sulfide. Hence bismuth sulfide additive plays a vital role in reduction of magnetite during charging of the iron electrode and prevents the formation of magnetite during the discharge of iron electrode. However, the presence of magnetite phase in the fully-formed and charged PAM iron electrode with bismuth sulfide suggests that PAM is not completely utilized during formation cycles.

*In situ electrochemical and XRD characterization of CGAM Fe electrode with Bi<sub>2</sub>S<sub>3</sub>.*— Constant-current discharge data during the first and second steps for CGAM iron electrode with bismuth sulfide are shown in Figs. 13a and 13b. The iron electrode delivers a capacity of 383 mAh/g and 293 mAh/g during first and second step of discharge, respectively. The (\*) marks in the figures show the state-of-charge values for which the in situ XRD patterns are recorded. The increase in capacity of these electrodes compared to the PAM electrode with bismuth sulfide is attributed to carbon grafting into the active material. In situ XRD recorded for fully-formed CGAM iron electrode with bismuth sulfide in fully charged condition at OCP, at end of 1<sup>st</sup> step and 2<sup>nd</sup> step of discharge are shown in Figs. 14a–14c. In situ XRD at OCP in fully charged condition shows the presence of only  $\alpha$ -iron and ferrous hydroxide phases with increased intensity in reflections from  $\alpha$ -iron phases. It is interesting to note that the reflections due to magnetite are not observed in these electrodes indicating complete reduction of magnetite present in CGAM. Accordingly, carbon grafting into the active material promotes the utilization of active material and results in increased capacity of the electrode. In situ XRD pattern at the end of 1<sup>st</sup> step discharge shows the presence of  $\alpha$ -iron and ferrous hydroxide phases. However, the intensity of the reflections from the crystal planes of ferrous hydroxide increases while intensity of the reflections from the crystal planes of  $\alpha$ -iron decreases. This suggests that the first step of discharge for electrode with bismuth sulfide is in accordance with Eq. 1. In situ XRD pattern at the end of 2<sup>nd</sup> step of discharge shows the presence of  $\alpha$ -iron and magnetite phases only with traces of iron oxy-hydroxide. This suggests that ferrous

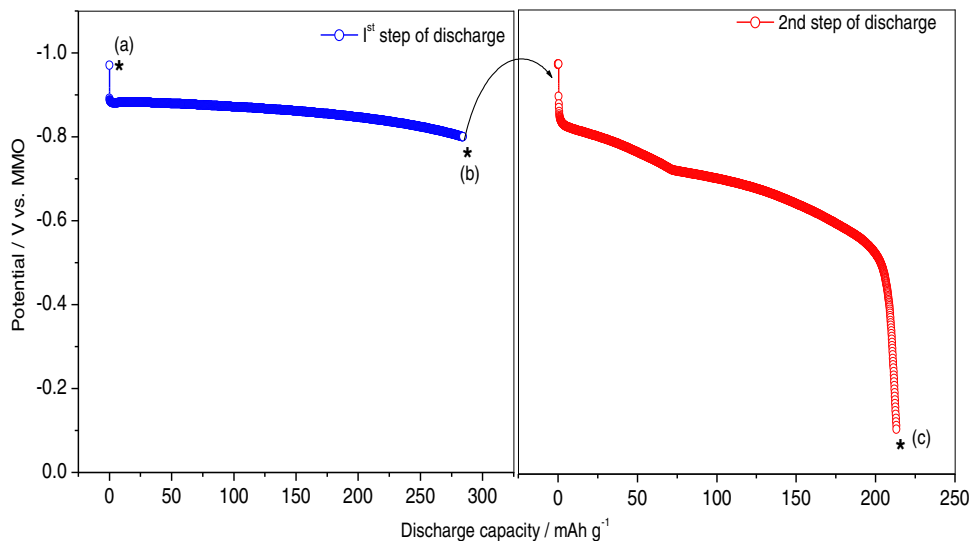


**Figure 11.** Constant-current discharge for PAM iron electrodes with bismuth sulfide at 40 mA in the in situ XRD cell.

hydroxide formed during the first discharge step is oxidized to magnetite. Figs. 15a and 15b show in situ XRD for CGAM iron electrode at various SoC values during first and second step of discharge, respectively. It is clearly observed that  $\alpha$ -iron is oxidized gradually to ferrous hydroxide during the first step of discharge. During the second step of discharge, both  $\alpha$ -iron and ferrous hydroxide are oxidized to magnetite. Fig. 16 shows in situ XRD pattern during charge of the deeply discharged CGAM iron electrodes by potentiostatic polarization in cathodic direction at varying potentials. It is observed that magnetite is reduced first to ferrous hydroxide at  $-1.0$  V and subsequently to  $\alpha$ -iron at cathode potentials exceeding  $-1.0$  V.

*Mechanism involving the role of  $\text{Bi}_2\text{S}_3$  for iron electrode reactions from in situ electrochemical and XRD studies.*— Various compounds present in fully-formed PAM and CGAM iron electrodes at SoC  $\sim 100\%$ , at the end of 1<sup>st</sup> and 2<sup>nd</sup> discharge are listed in Table II. It is observed from the data in the table that bismuth sulfide additive present in PAM iron electrode catalyses reduction of magnetite present in the active material to  $\alpha$ -iron. However, magnetite is not utilized fully during formation cycles. When carbon is grafted into the active material as in CGAM iron electrode, magnetite phase is completely utilized and reduced to  $\alpha$ -iron. This is attributed to increased utilization of CGAM due to the uniform distribution of carbon grafted into the

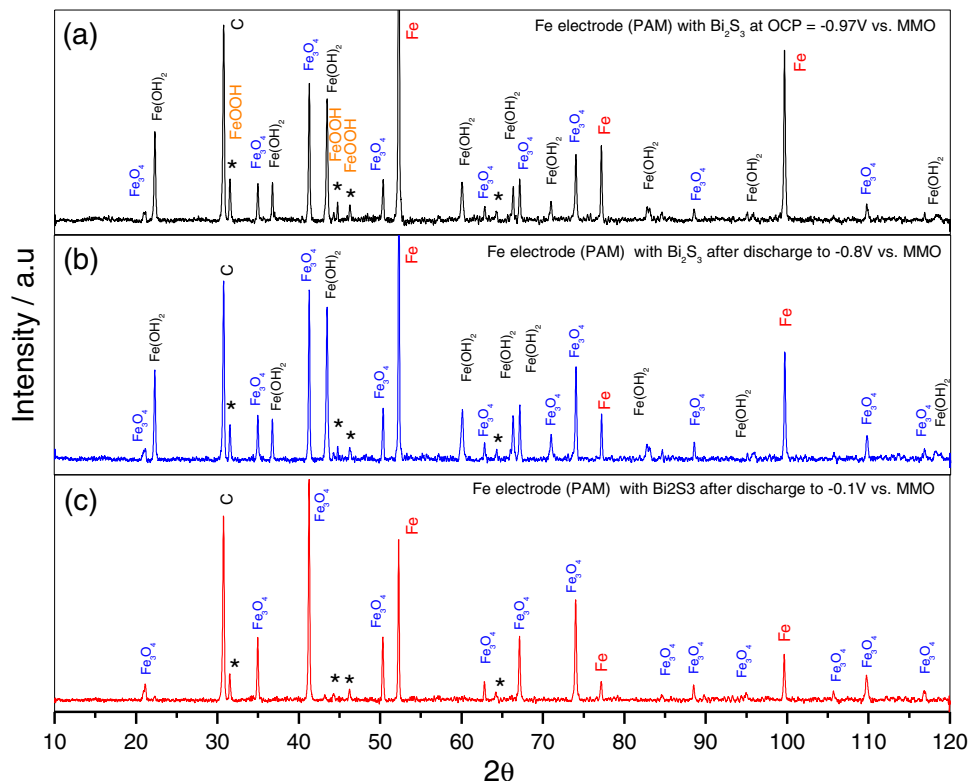


**Figure 12.** In situ XRD for PAM iron electrode during constant current discharge at (a) OCP, (b) after discharge to  $-0.8$  V vs. MMO, and (c) after discharge to  $-0.1$  V vs. MMO.

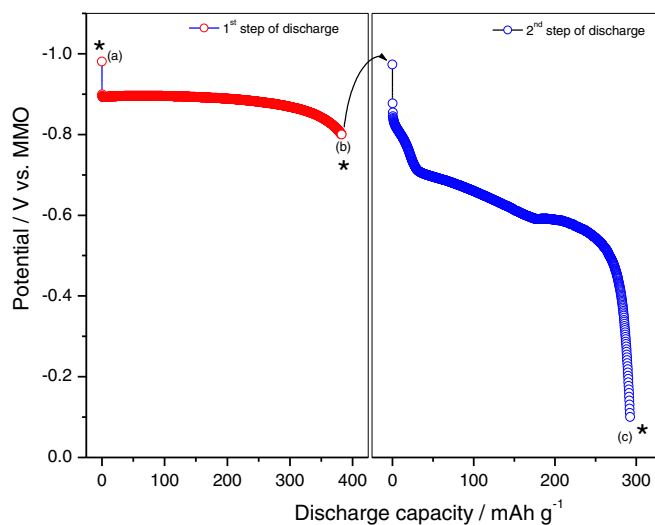


**Figure 13.** Constant-current discharge curves of CGAM iron electrodes with bismuth sulfide at 40 mA in the in situ XRD cell.

active material. This accounts for the observed increase in the capacity of the CGAM iron electrode compared to PAM iron electrodes. It is important to note that bismuth sulfide additive catalyses the reduction of magnetite while charging iron electrode and facilitates the precip-

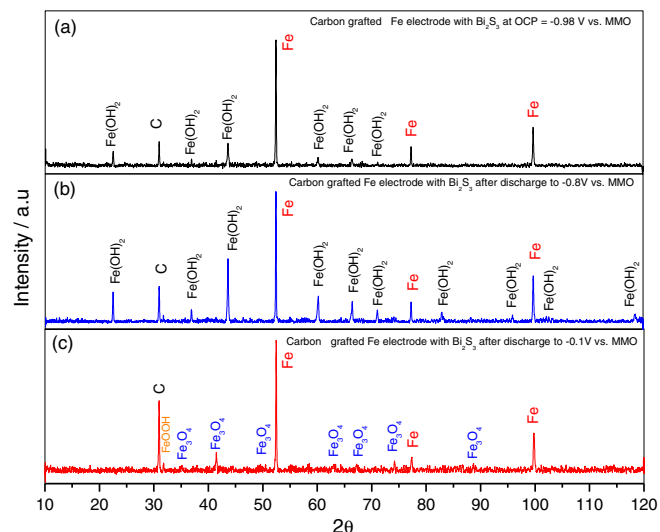


**Figure 14.** In situ XRD for Carbon grafted electrode with bismuth sulfide during constant current discharge at (a) OCP, (b) after discharge to  $-0.8$  V vs. MMO, and (c) after discharge to  $-0.1$  V vs. MMO.

itation of ferrous hydroxide as the product during the first discharge step by preventing the formation of passive magnetite. This suggests that bismuth sulfide additive has bi-functional role in alkaline iron electrodes.

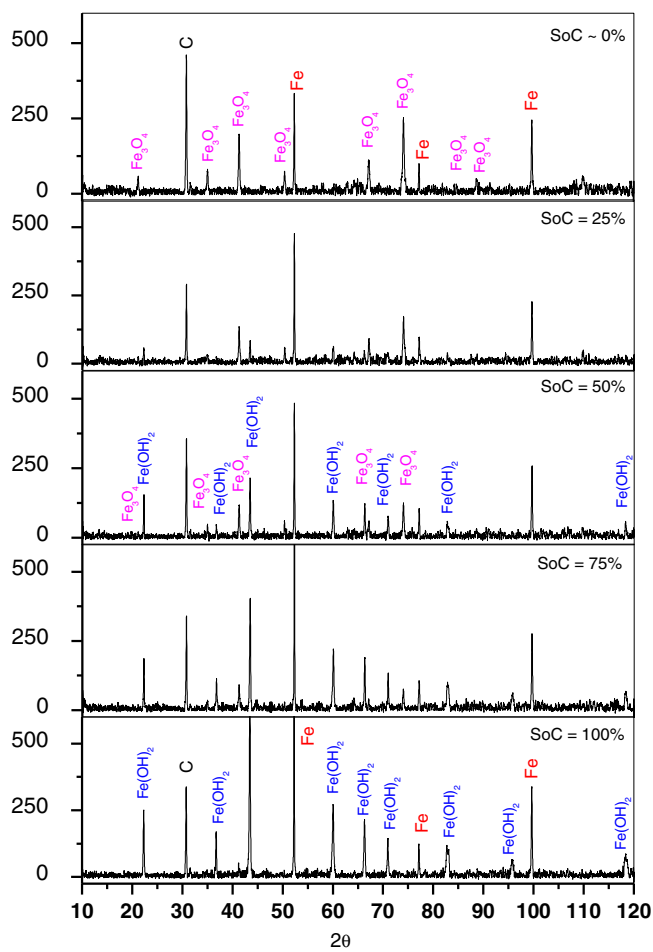
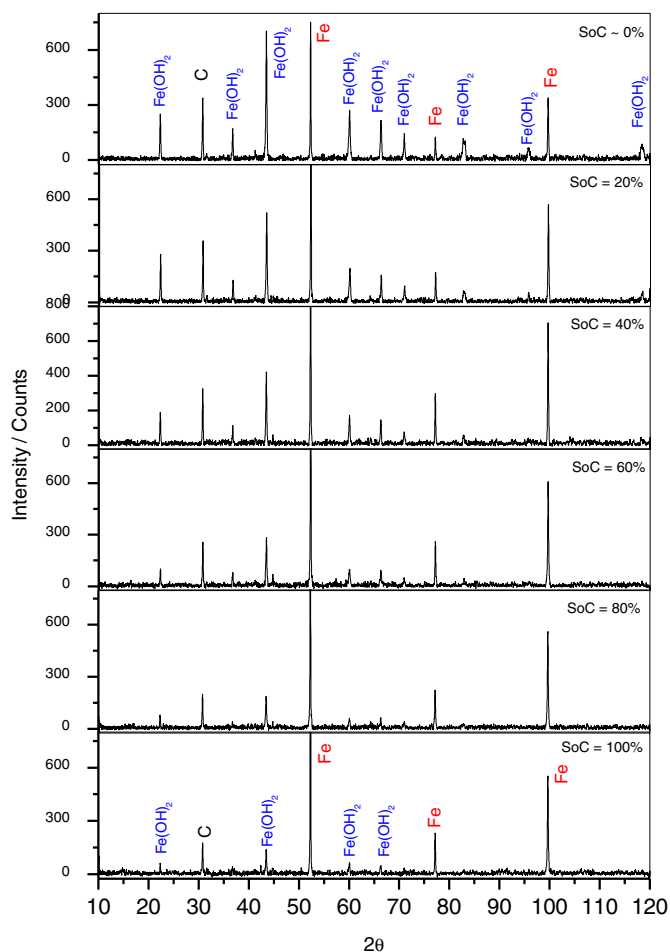


**Figure 15.** In situ XRD for CGAM Fe electrode at various SoC during constant current discharge.

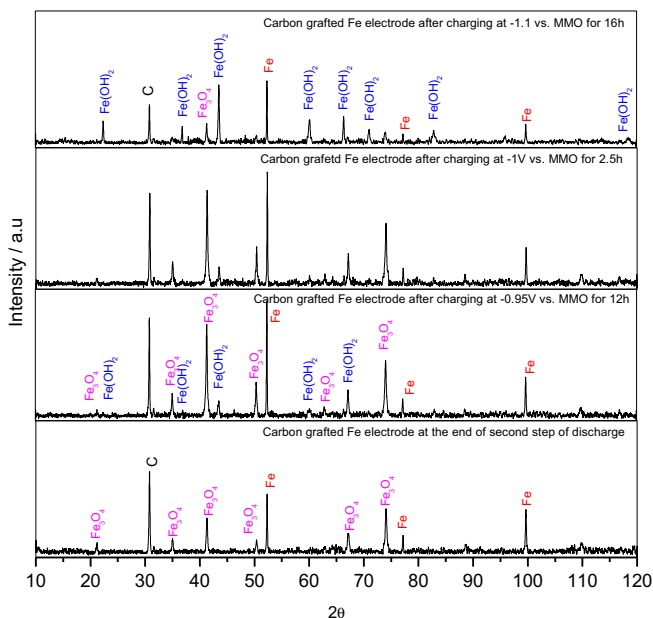
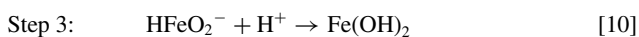
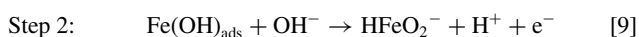
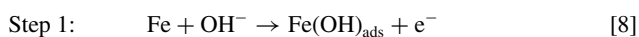


**Figure 16.** In situ XRD for Carbon grafted iron electrode with bismuth sulfide during potentiostatic polarization in cathodic direction.

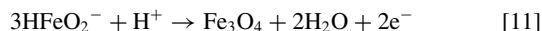
*Mechanism for discharge reaction of the iron electrode.*— The reaction mechanism based on the results from in situ electrochemical and XRD patterns for the iron electrodes prepared from PAM and CGAM is envisaged as follows.

Mechanism for Fe electrode for first step of discharge reaction takes place in three steps as:



Porous iron electrodes in charged state have metallic iron in body centered cubic crystal structure.  $\text{OH}^-$  ions of the electrolyte, present in the pores of the electrode, first react with the metallic iron forming  $\text{Fe(OH)}_{\text{ads}}$  intermediates as in Eq. 8. When these intermediate species further undergo oxidation in presence of  $\text{OH}^-$  ions,  $\text{Fe(OH)}_{\text{ads}}$  intermediate dissolve into the solution as  $\text{HFeO}_2^-$  ions and  $\text{H}^+$  ions. Subsequently,  $\text{HFeO}_2^-$  is precipitated as ferrous hydroxide. It is found that ferrous hydroxide is formed in hexagonal crystal structure. As the reaction progresses,  $\text{OH}^-$  ions concentration in the pores depletes during second discharge step as represented in Eq. 9 with an increase in the  $\text{H}^+$  ion activity. Hence, ferrous hydroxide formed as crystalline product is unstable and dissolves into the solution present in the pores. In such an environment, the dissolved  $\text{HFeO}_2^-$  ions are susceptible to further oxidation. Hence,  $\text{H}^+$  ion activity needs to be reduced to

stabilize ferrous hydroxide. In the case of PAM iron electrode without bismuth sulfide additive, ferrous hydroxide phase is not observed both after galvanostatic and potentiostatic polarization of Fe electrode suggesting that ferrous hydroxide could be present in amorphous state and could easily dissolve into the solution resulting in further oxidation of  $\text{HFeO}_2^-$  to magnetite. This can be represented as:



However, in the presence of bismuth sulfide additive, PAM and CGAM electrodes show the presence of crystalline ferrous hydroxide suggesting that bismuth sulfide additive helps stabilizing ferrous hydroxide which is precipitated as a crystalline product. In an earlier paper,<sup>12</sup> we have reported that the bismuth sulfide added to the electrode is reduced to elemental bismuth according to Eq. 12



This leaves the sulfide ions adsorbed onto the iron electrode. In the literature, it is reported that the adsorbed sulfur or sulfide ions have following effects: (a) increase anodic dissolution with increased stability of adsorbed sulfide on the surface due to weakening of the metal – metal bonds induced by adsorbed sulfur leading to the decrease of activation energy for dissolution, (b) prevent passivation by blocking sites for adsorption of hydroxyl ions and (c) induce the breakdown of passive film of metal oxides due to weakening of bonding of the oxide to the substrate.<sup>19</sup> It is reported that even small quantities of sulfur or sulfide ions adsorbed at the surface in monolayer or sub-monolayer levels promote dissolution of macroscopic amounts of materials and retard passivation.<sup>19</sup> In iron electrodes with bismuth sulfide also such effects are observed. In our earlier study, we have reported that the bismuth sulfide added to the PAM iron electrode decreases the activation energy barrier for iron – dissolution from  $35.5 \text{ kJmol}^{-1}$  to  $11.5 \text{ kJmol}^{-1}$ .<sup>20</sup> These findings suggest that there is atomic level interaction between adsorbed sulfide ions with metal atoms and ions of the electrolyte at the interface.

Potential – pH diagrams for Fe –  $\text{H}_2\text{O}$ , S –  $\text{H}_2\text{O}$  and S adsorbed on Fe constructed using thermodynamic data allow us to predict thermodynamically stable ions and compounds in the potential region where the iron electrodes are used. In the literature,<sup>21–23</sup> potential – pH diagram for  $\text{FeS}_{\text{ads}}$  – water is reported for different sulfur coverage values, namely at  $\theta = 0.01, 0.5$  and  $0.99$ , at dissolved sulfur concentration of  $10^{-4} \text{ mol/kg}$ . The potential – pH diagram for S –  $\text{H}_2\text{O}$  suggest that  $2.52 \times 10^{-5} \text{ mol}$  of elemental sulfur could be formed from  $\text{H}_2\text{S}$ . In the present study, when 1 wt% of  $\text{Bi}_2\text{S}_3$  in the iron electrode is reduced to elemental bismuth, it will liberate  $5.8 \times 10^{-5} \text{ mol}$  of sulfide ions. According to Eq. 5, protons are liberated into the solution when iron electrode undergoes discharge. The concentration of the proton depends on the magnitude of the discharge current. At a typical discharge current of 200 mA, according to the Eqs. 4 and 5, protons are liberated at a rate of  $\sim 1.03 \times 10^{-6} \text{ mol/s}$ . Since the concentration of the sulfide ions and protons are nearly similar, it is believed that sulfide ions play a vital role in controlling the activity of protons. To further elucidate this aspect, the potential – pH diagrams for Fe –  $\text{H}_2\text{O}$ , S- $\text{H}_2\text{O}$  and  $\text{FeS}_{\text{ads}}$  – water are superimposed as shown in Figs. 17 and 18. From these potential – pH diagrams, it can be inferred that  $\text{HS}^-$ ,  $\text{FeS}_{\text{ads}}$ ,  $\text{OH}^-$ , and  $\text{H}_2\text{O}$  are stable species in the potential and pH regimes where alkaline iron electrodes are used. Also, it is observed that the following chemical and electrochemical reactions could be

**Table II.** Discharge products as identified from in situ XRD.

Electrodes	Powdered active material	As prepared electrode at OCP-0.97 V vs. MMO	SoC ~ 100% at OCP -0.97 V vs. MMO	End of 1 <sup>st</sup> step at -0.8 V vs. MMO	End of 2 <sup>nd</sup> step at -0.1 V vs. MMO
PAM	Fe, Fe <sub>3</sub> O <sub>4</sub>	Fe, Fe <sub>3</sub> O <sub>4</sub>	Fe, Fe <sub>3</sub> O <sub>4</sub>	Fe, Fe <sub>3</sub> O <sub>4</sub>	Fe, Fe <sub>3</sub> O <sub>4</sub>
PAM + Bi <sub>2</sub> S <sub>3</sub>	Fe, Fe <sub>3</sub> O <sub>4</sub>	Fe, Fe <sub>3</sub> O <sub>4</sub>	Fe, Fe <sub>3</sub> O <sub>4</sub> , Fe(OH) <sub>2</sub> , and FeOOH	Fe, Fe <sub>3</sub> O <sub>4</sub> , Fe(OH) <sub>2</sub> , and FeOOH	Fe, Fe <sub>3</sub> O <sub>4</sub> , and FeOOH
CGAM + Bi <sub>2</sub> S <sub>3</sub>	Fe, Fe <sub>3</sub> O <sub>4</sub>	Fe, Fe <sub>3</sub> O <sub>4</sub>	Fe, Fe(OH) <sub>2</sub>	Fe, Fe(OH) <sub>2</sub>	Fe, Fe <sub>3</sub> O <sub>4</sub> , and FeOOH

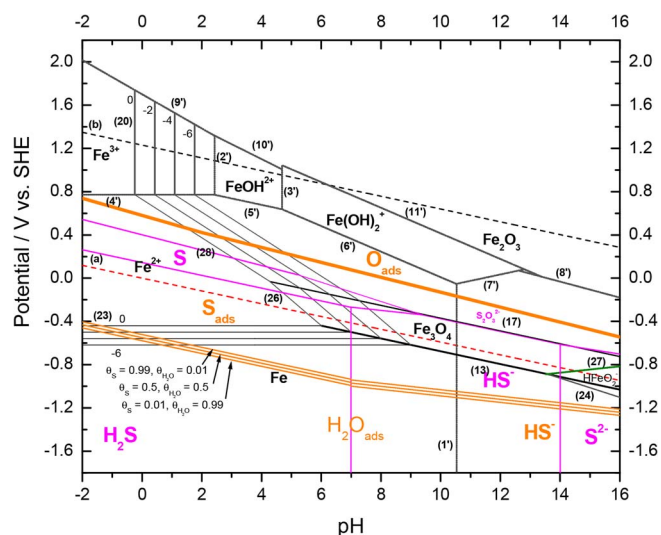
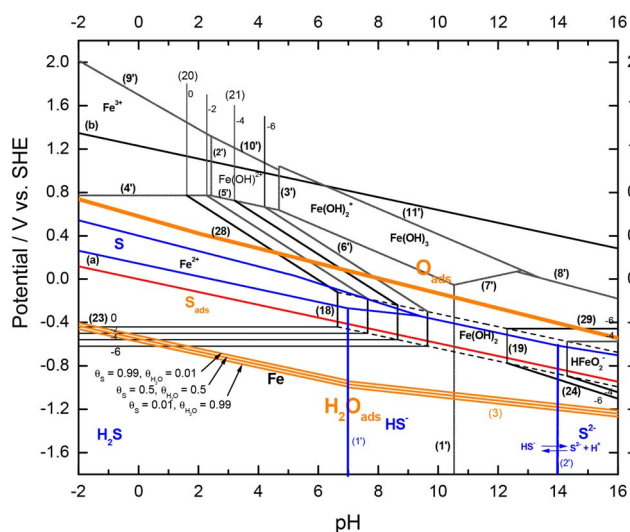
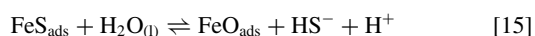
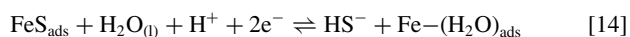


**Figure 17.** Superimposed potential – pH diagram for Fe – H<sub>2</sub>O with Fe, Fe(OH)<sub>2</sub>, S – H<sub>2</sub>O and Fe – S<sub>ads</sub> – Water.

**Figure 18.** Superimposed potential – pH diagram for Fe – H<sub>2</sub>O with Magnetite, S – H<sub>2</sub>O and Fe – S<sub>ads</sub> – Water system.

possible.



Eq. 13 is a possible chemical reaction occurring at pH ≈ 14. Eqs. 14 and 15 act as source of HS<sup>-</sup> ions. The existence of such equilibrium could act as a buffer in the pores of the iron electrode and hence could control the pH of the electrolyte. As a result, HFeO<sub>2</sub><sup>-</sup> ions could

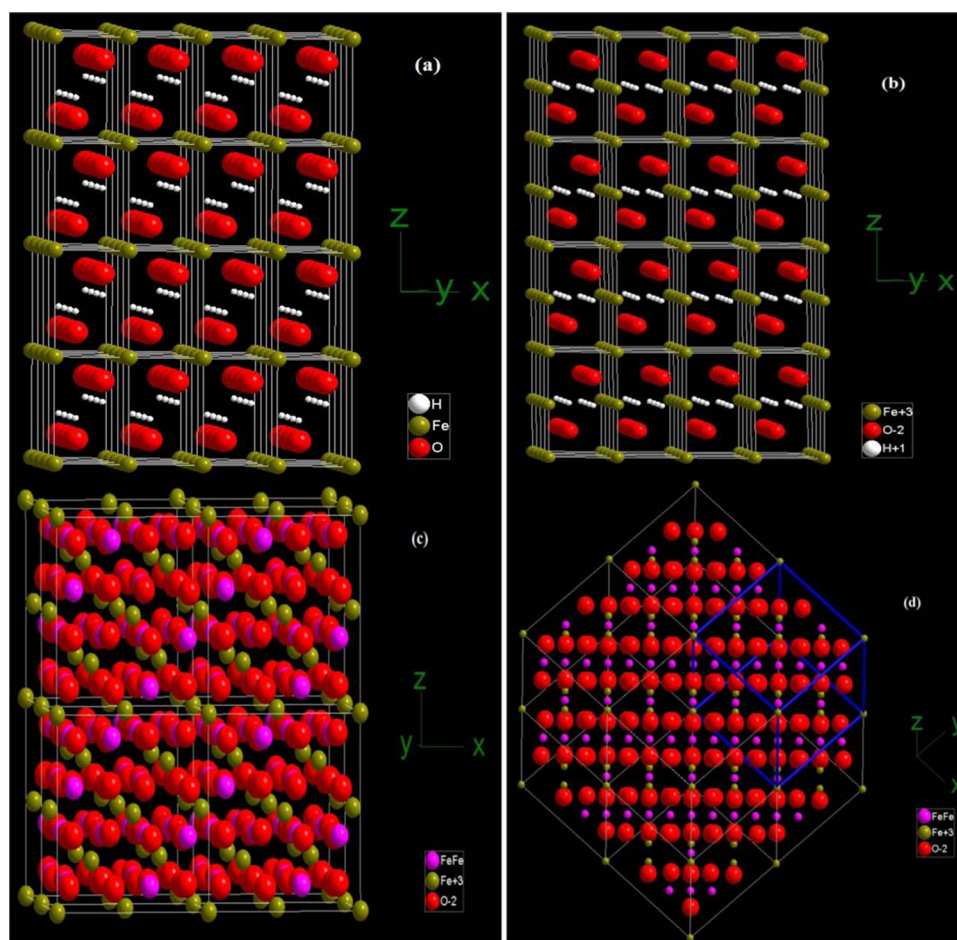


**Figure 19.** Crystal lattice structure for (a) Fe(OH)<sub>2</sub>, (b) FeOOH, (c) and (d) Magnetite.

precipitate according to Eq. 16.

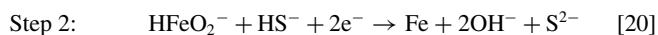
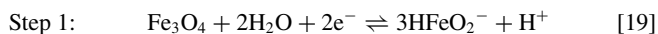


During second step of discharge of Fe electrode by homogeneous mechanism, oxidation of  $\text{Fe}^{2+}$  to  $\text{Fe}^{3+}$  with de-intercalation of  $\text{H}^+$  ions occurs as shown below.



Such a solid state reaction is possible since ferrous hydroxide has a layered structure akin to  $\text{CdI}_2$  as shown in Fig. 19a. Ferrous hydroxide has hexagonal closed packing of oxygen ions with  $\text{Fe}^{2+}$  ions occupying the octahedral holes in alternate layers with hydrogen ions present in between two oxygen ion layers. Upon oxidation of  $\text{Fe}^{2+}$  to  $\text{Fe}^{3+}$  state, a proton could de-intercalate from the layered structure resulting in the formation of iron oxy-hydroxide leaving  $\text{Fe}^{3+}$  ions in octahedral holes in the alternate layers as shown in Fig. 19b. However, hydrogen ions during diffusion through layered structure are de-intercalated as hydronium ions ( $\text{H}_3\text{O}^+$ ) as hydrogen ions always prefer to be solvated. Accordingly, iron oxy-hydroxide phase will only be an intermediate phase and the dehydration results in the formation of magnetite as shown in Figs. 19c and 19d.

During charge, the iron electrodes after deep discharge and during formation cycles, exhibit reduction of magnetite to metallic iron. This takes place in two steps. Magnetite is first reduced to  $\text{HFeO}_2^-$  ion which is precipitated as ferrous hydroxide depending on the potential or it may get reduced to  $\alpha$ -iron. It is noteworthy that the reduction of passive magnetite to  $\text{HFeO}_2^-$  requires  $\text{H}^+$  ions in highly alkaline solution as shown below.



### Conclusions

Ameliorating effect of carbon grafting into the iron active material on the kinetics, and mechanism of charge and discharge reactions of rechargeable-alkaline-iron electrodes with and without bismuth sulfide additive as probed by in situ X-ray diffraction in conjunction with Extended X-ray Absorption Fine Structure (EXAFS) and electrochemistry is studied. EXAFS data unravel that the pristine active material (PAM) comprises 87% of magnetite and 13% of  $\alpha$ -iron while carbon grafted active material comprises 60% of magnetite and 40% of  $\alpha$ -iron. In situ XRD study shows that magnetite present in PAM iron electrode without bismuth sulfide is not reduced during charging whereas PAM iron electrode with bismuth sulfide additives is partially reduced to  $\alpha$ -Fe/ $\text{Fe(OH)}_2$ . Interestingly, carbon-grafted iron electrodes with bismuth sulfide exhibit complete conversion of magnetite to  $\alpha$ -Fe/ $\text{Fe(OH)}_2$  and, consequently, it is surmised that carbon grafting into iron active material promotes utilization of active material. The promotional effect of carbon is further substantiated from electrode kinetics parameters obtained from steady-state potentiostatic polarization and tafel plots. The steady-state potentiostatic polarization data show that addition of bismuth sulfide increases critical current for Fe electrodes during anodic direction of polarization without any significant change in passivation potential suggesting that sulfide additive increases the anodic dissolution of Fe metal. Carbon grafting

into the active material increases the critical current indicating that carbon promotes utilization of active material. Tafel data shows no significant change due to carbon grafting. In situ XRD studies show that the PAM iron electrodes without bismuth sulfide do not form crystalline ferrous hydroxide when discharged at  $100 \text{ mA g}^{-1}$  current density but are directly oxidized to more passive magnetite. Bismuth sulfide added to active materials catalyzes the reduction of magnetite during charging of the iron electrodes and promotes the dissolution – precipitation of iron during the first step of discharge. In situ XRD data also corroborate that bismuth sulfide has ameliorating effect on charging and discharging reactions of iron electrodes. Beneficial effects of bismuth sulfide additives are that: (a) it catalyzes the reduction of magnetite to metallic  $\alpha$ -iron and hence the capacity of iron electrode is increased, (b) it stabilizes and facilitates precipitation of ferrous hydroxide, (c) it prevents the formation of magnetite during the first step of discharge reaction, and (d) it increases the cycle life of iron electrodes. The superimposed potential – pH diagrams for  $\text{Fe} - \text{H}_2\text{O}$ ,  $\text{S} - \text{H}_2\text{O}$  and  $\text{S}_{\text{ads}} - \text{H}_2\text{O}$  constructed from the thermodynamic data suggest that the existence of chemical equilibrium  $\text{HS}^- \rightleftharpoons \text{S}^{2-} + \text{H}^+$  at  $\text{pH} \approx 14$ , independent of the potential region where iron electrodes are operated, acts as buffer and promotes the charge and discharge reactions of iron.

### Acknowledgments

We gratefully acknowledge the financial support from Department of Science & Technology, Government of India, New Delhi. KRP acknowledges beam time and travel support for XAFS experiments from RRCAT, Indore, and help from Dr. S. N. Jha and Kapil Ingle in the measurements.

### References

- D. Linden and T. B. Reddy, Eds., *Handbook of Batteries*, Third Edition, McGraw – Hill, pp. 25.3 (2001).
- H. Wang, Y. Liang, M. Gong, Y. Li, W. Chang, T. Mefford, J. Zhou, J. Wang, T. Regier, F. Wei, and H. Dai, *Nat. Commun.*, **3** 917 (2012)
- A. J. Salkind, C. J. Venuto, and S. Uno Falk, *J. Electrochem. Soc.*, **111**, 493 (1964).
- S. Hills, *J. Electrochem. Soc.*, **112**, 1048 (1965).
- D. W. Shoesmith, P. Taylor, M. G. Bailey, and B. Ikeda, *Electrochim. Acta*, **23** 903 (1978).
- K. Micka and Z. Zábanský, *J. Power Sources*, **19**, 315 (1987).
- U. Casellato, N. Comisso, and G. Mengoli, *Electrochim. Acta*, **51**, 5669 (2006).
- A. A. Kamnev, *Electrochim. Acta*, **41**, 267 (1996).
- T. S. Balasubramanian, K. Vijayamohan, and A. K. Shukla, *J. Appl. Electrochem.*, **23**, 947 (1993).
- A. K. Manohar, S. Malkhandi, B. Yang, C. Yang, G. K. Surya Prakash, and S. R. Narayanan, *J. Electrochem. Soc.*, **159A**, 1209 (2012).
- B. T. Hang, S.-H. Yoon, S. Okada, and J.-I. Yamaki, *J. Power Sources*, **168**, 522 (2007).
- A. Sundar Rajan, S. Sampath, and A. K. Shukla, *Energy Environ. Sci.*, **7**, 1110 (2014).
- A. K. Manohar, C. Yang, and S. R. Narayanan, *J. Electrochem. Soc.*, **162**(9) A1864 (2015).
- A. J. Bard and L. R. Faulkner, *Electrochemical Methods Fundamentals and Applications*, Second Edition, John Wiley & Sons, Inc. 2001.
- B. Ravel and M. Newville, *J. Synchrotron Rad.*, **12**, 537 (2005).
- S. I. Zabinsky, J. J. Rehr, A. Ankudinov, R. C. Albers, and M. J. Eller, *Phys. Rev. B*, **52**, 2995 (1995).
- A. K. Shukla, M. K. Ravikumar, A. Sundar Rajan, and T. N. Guru Row, Indian Pat., Application No. 6225/CHE/2014 (2014).
- H. G. Silver and E. Lekas, *J. Electrochem. Soc.*, **117**(1) 5 (1970).
- P. Marcus, "Corrosion Mechanisms in Theory and Practice" edited by Marcel Dekker, Inc., NY, pp 287 (2002).
- M. K. Ravikumar, T. S. Balasubramanian, and A. K. Shukla, *J. Appl. Electrochem.*, **26**, 1111 (1996).
- R. Winston Revie, Ed., "Uhlig's Corrosion Handbook", Second Edition, John Wiley & Sons, Inc., pp. 111 (2000).
- P. Marcus and E. Protopopoff, *J. Electrochem. Soc.*, **137**, 2709 (1990).
- M. Pourbaix and A. Pourbaix, *Geochim. Cosmochim. Acta*, **56**, 3157 (1992).